

Shallow-velocity models at the Kilauea Volcano, Hawaii, determined from array analyses of tremor wavefields

Gilberto Saccorotti,¹ Bernard Chouet² and Phillip Dawson²

¹Istituto Nazionale di Geofisica e Vulcanologia, Osservatorio Vesuviano Via Diocleziano 328, 80124 Napoli, Italy. E-mail: gilberto@ov.ingv.it

²US Geological Survey, 345 Middlefield Road, MS 910, Menlo Park, CA 94025

Accepted 2002 September 6. Received 2002 August 12; in original form 2002 February 1

SUMMARY

The properties of the surface wavefield at Kilauea Volcano are analysed using data from small-aperture arrays of short-period seismometers deployed in and around the Kilauea caldera. Tremor recordings were obtained during two Japan–US cooperative experiments conducted in 1996 and 1997. The seismometers were deployed in three semi-circular arrays with apertures of 300, 300 and 400 m, and a linear array with length of 1680 m. Data are analysed using a spatio-temporal correlation technique well suited for the study of the stationary stochastic wavefields of Rayleigh and Love waves associated with volcanic activity and scattering sources distributed in and around the summit caldera. Spatial autocorrelation coefficients are obtained as a function of frequency and are inverted for the dispersion characteristics of Rayleigh and Love waves using a grid search that seeks phase velocities for which the L-2 norm between data and forward modelling operators is minimized. Within the caldera, the phase velocities of Rayleigh waves range from 1400 to 1800 m s⁻¹ at 1 Hz down to 300–400 m s⁻¹ at 10 Hz, and the phase velocities of Love waves range from 2600 to 400 m s⁻¹ within the same frequency band. Outside the caldera, Rayleigh wave velocities range from 1800 to 1600 m s⁻¹ at 1 Hz down to 260–360 m s⁻¹ at 10 Hz, and Love wave velocities range from 600 to 150 m s⁻¹ within the same frequency band. The dispersion curves are inverted for velocity structure beneath each array, assuming these dispersions represent the fundamental modes of Rayleigh and Love waves. The velocity structures observed at different array sites are consistent with results from a recent 3-D traveltimes tomography of the caldera region, and point to a marked velocity discontinuity associated with the southern caldera boundary.

Key words: calderas, seismic velocities, surface waves, volcanic structure.

INTRODUCTION

During the past decade volcano seismology has made substantial progress toward a quantitative understanding of the physical processes operating in magmatic and hydrothermal environments. Major advances include an improved ability to locate emergent and/or sustained signals such as long-period (LP) events and tremor (e.g. Furumoto *et al.* 1990; Yamaoka *et al.* 1991; Goldstein & Chouet 1994; Chouet *et al.* 1997; Saccorotti *et al.* 1998; Almendros *et al.* 2001), and the full inversion of very-long-period (VLP) waveforms for moment tensor components of volcanic sources (e.g. Chouet & Dawson 1997; Ohminato *et al.* 1998; Nishimura *et al.* 2000; Chouet *et al.* 2002). The resolution and reliability of these methods mostly depend upon the accuracy of ray tracing (in the case of array-based source locations), or Green function calculations (in the case of complete waveform modelling), which in turn rely on a detailed knowledge of the physical properties of the propagation medium.

The seismic approach to modelling volcanic velocity structures has relied chiefly on traveltimes tomography using either natural

sources (e.g. Benz 1996; Okubo *et al.* 1997; Dawson *et al.* 1999; Chiarabba *et al.* 2000) or artificial sources (e.g. Zollo *et al.* 1996). Tomography can yield images of a volcanic velocity structure down to scalelengths of the order of 500 m (Dawson *et al.* 1999), sufficient for the identification of gross structural features in a volcanic edifice, including anomalous zones marking the presence of molten rocks and hydrothermalized materials. This level of resolution is adequate for the evaluation of Green functions at periods in the 1–100 s range. Finer resolution of the velocity structure is required to model short-period (<1 s) wave propagation.

Recent results in seismic engineering (Liu *et al.* 2000; Louie 2001; Bettig *et al.* 2001) have demonstrated that inversions of dispersion data based on analyses of seismic noise wavefields can constrain shallow shear wave velocity structures with a minimum level of uncertainty. This approach is attractive and economic as it relies on the background seismic noise and does not require any particular source. Earlier analyses of the dispersive properties of surface waves in active volcanoes were performed by Ferrazzini *et al.* (1991) at the Puu Oo crater, Hawaii; Métaixian *et al.* (1997) at the Masaya

Volcano, Nicaragua; Chouet *et al.* (1998) at the Stromboli Volcano, Italy; Saccorotti *et al.* (2001a) at the Deception Island Volcano, Antarctica; and Saccorotti *et al.* (2001c) at the Vesuvius Volcano, Italy.

In this paper we apply the spatial correlation technique of Aki (1957, 1965) for the analysis of stochastic wavefields, to derive the dispersive properties of the surface wave components in the tremor wavefield at the Kilauea Volcano, Hawaii. We use data collected during two separate seismic experiments conducted in 1996 and 1997 within the framework of a Japan–US agreement for technical and scientific cooperation. The dispersion data are used to derive the shallow shear wave velocity structure beneath each array site. We start with a brief overview of the activity of Kilauea Volcano at the times of the two experiments, and the description of the arrays and data recorded. We follow with a review of Aki's correlation method and proceed with inversions of the correlation data for the dispersion characteristics of Rayleigh and Love waves. We use the dispersion data to obtain velocity models beneath each array, and discuss these models within the structural framework of the caldera.

KILAUEA VOLCANO

Kilauea Volcano is one the most active volcanoes in the world. Its current eruptive activity, which began in 1983 January, has been marked by three distinct phases, each consisting of multiple eruptive episodes. The third and ongoing phase began on 1992 February 17, and is characterized by gentle, sustained effusive emissions from several vents in the proximity of the Puu Oo–Kupaianaha fracture system on the east rift approximately 20 km from the summit caldera.

From these effusive centres lava flows to the seashore along a 13 km long tube and channel system.

The occurrence of volcanic tremor is routinely documented by the Hawaiian Volcano Observatory (HVO). On the basis of measurements of signal amplitudes and areal extent of detection by the seismic network, HVO scientists subdivide tremor into three categories of inferred depth: shallow (<5 km), intermediate (5–25 km) and deep (30–60 km) (Koyanagi *et al.* 1987). A common source is inferred for LP events and tremors based on the similarities observed in their spectral features, times of occurrence and the spatial attenuation of signal amplitudes. LP events with identifiable onset times are located using the standard earthquake location method and yield information concerning the hypocentral region of tremor.

Shallow tremors are often observed near an eruption site, where tremor amplitudes are found to correlate reasonably well with changes in lava extrusion rates and/or fountaining intensities (Koyanagi *et al.* 1987). Initial efforts towards a quantitative assessment of tremor wavefields were focused on such shallow sources associated with eruptive activity at the Puu Oo vent on the eastern rift of Kilauea (Ferrazzini *et al.* 1991; Goldstein & Chouet 1994). More recent quantitative descriptions of the location and spatial extent of sources of shallow tremor far from an eruptive site were obtained by Saccorotti *et al.* (2001b). The most detailed 3-D image of a shallow tremor source was obtained by Almendros *et al.* (2001), who analysed data from the Kilauea Volcano using a multi-array location technique. Results from the latter two studies suggest that the data analysed in the present paper are representative of a shallow (<1 km) source of tremor located beneath the northeast edge of the Halemaumau pit crater (see Fig. 1).

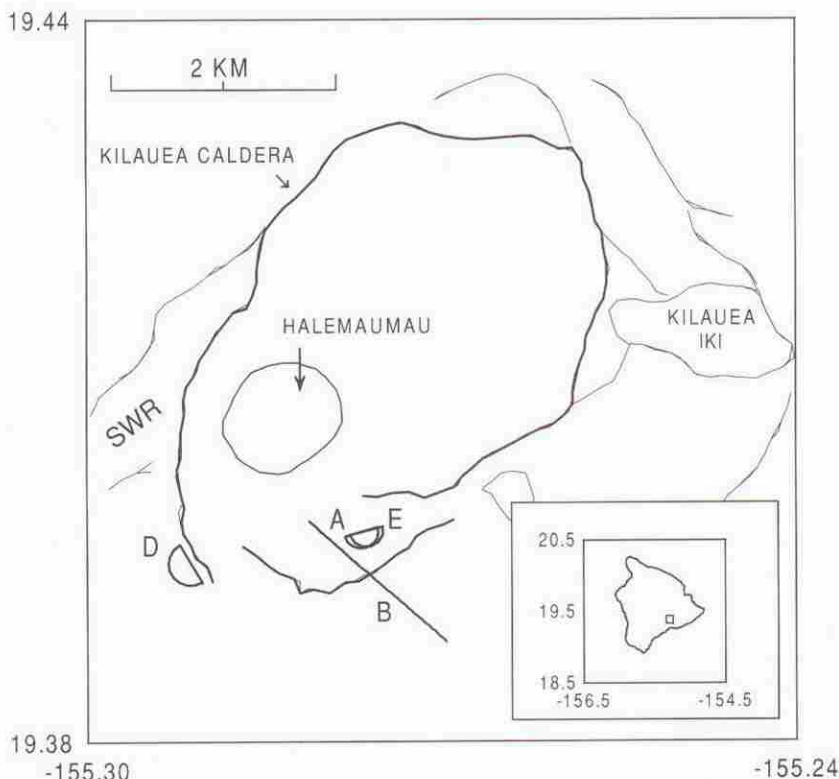


Figure 1. Map of the Kilauea summit caldera. The three semi-circles and line segment outline dense arrays deployed during the 1996 and 1997 field surveys. The A and B arrays were part of the 1996 deployment, and the D and E arrays were part of the 1997 deployment. Bold lines outline the boundaries of the caldera. Thin lines indicate ring fractures and pit craters. SWR indicates the southwest rift zone. The east rift zone extends out of the map east-southeast of the Kilauea Iki pit crater. The square in the inset map shows the position of Kilauea on the island of Hawaii.

INSTRUMENTATION AND DATA

The data used in this study were recorded during two separate large-scale seismic experiments conducted by a joint Japan-US team in 1996 (McNutt *et al.* 1997; Saccorotti *et al.* 2001b) and 1997 (Almendros *et al.* 2001). The purpose of these experiments was to investigate the wavefield composition and source properties of volcanic signals associated with the ongoing eruptive activity at the Kilauea Volcano. Details of the seismic arrays set up in the 1996 experiment can be found in McNutt *et al.* (1997). Almendros *et al.* (2001) provide details of the instrument set up in the 1997 deployment.

Our data consist of tremors recorded on two small-aperture arrays deployed in 1996 and two small-aperture arrays deployed in 1997 (Fig. 1). Array A includes 31 three-component receivers deployed in a semi-circular spoked pattern with a station spacing of 50 m along

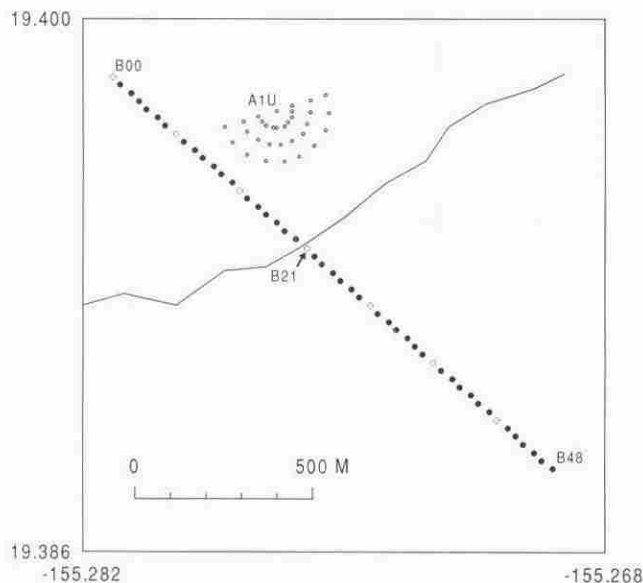


Figure 2. Configurations of the semi-circular array A with radius of 150 m, and linear array B with length of 1680 m deployed at Kilauea during the 1996 field survey. Solid dots indicate vertical-component sensors and open circles mark three-component sensors. The bold line marks the caldera boundary. Data from receivers B01–B20 in the linear array were processed separately from those of receivers B21–B48 in that array.

the spokes and angular spacing of 20° between spokes (Fig. 2). Array B consists of 42 vertical-component and seven three-component receivers deployed with a receiver spacing of 35 m along a line trending $N45^\circ W$ (Fig. 2). Array D consists of 41 three-component receivers deployed in a semi-circular spoked pattern with a station spacing of 50 m along the spokes and angular spacing of 20° between spokes (Fig. 3a). Array E consists of 22 vertical-component receivers deployed in a semi-circular spoked pattern with a station spacing of 50 m along the spokes and angular spacing of 30° between spokes (Fig. 3b).

All of the seismometers have a natural frequency of 2 Hz, a critical damping of 0.7 and sensitivity of $50 \text{ V m}^{-1} \text{ s}^{-1}$. Receiver positioning and time synchronization between array elements were obtained by GPS with respective accuracies of 1 cm and 5 μs . The data were sampled at 100 samples s^{-1} and recorded on 16 bit, three-channel Hakusan data loggers.

For our analyses we selected 27 min of tremor simultaneously recorded on arrays A and B, and 18 min of tremor simultaneously recorded on arrays D and E. Fig. 4 shows typical vertical-component seismograms and corresponding amplitude spectra recorded during the first minute of the selected time interval at receivers D00–D44 in array D (see Fig. 3a).

SPATIAL CORRELATION METHOD

The statistical correlation method of Aki (1957) is based on the critical assumption that the observed wavefield is stationary in time and space. The method provides a relation between the spectrum of the waves in time and their spectrum in space, from which the properties of the wavefield can be inferred. This method has been extensively described in earlier papers (e.g. Aki 1957; Ferrazzini *et al.* 1991; Chouet 1996; Métaxian *et al.* 1997; Chouet *et al.* 1998; Bettig *et al.* 2001), and in the following we limit our presentation to a brief review of the basic relationships used in applications of the method to the three modes of polarization of a 2-D wavefield.

We first define a normalized spatial autocorrelation coefficient between two receivers as

$$\rho(r, \varphi) = \frac{\langle u(x, y, t) \cdot u(x + r \cos \varphi, y + r \sin \varphi, t) \rangle}{\langle u(x, y, t) \cdot u(x, y, t) \rangle}, \quad (1)$$

where $\langle \rangle$ denotes averaging over time, (x, y) and $(x + r \cos \varphi, y + r \sin \varphi)$ are the Cartesian coordinates of the two receivers, r is the distance between the receivers and φ is the azimuth of the two

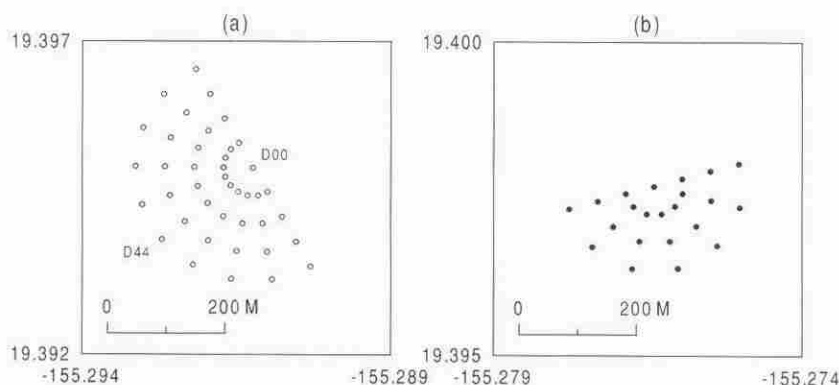


Figure 3. Configurations of the semi-circular arrays deployed during the 1997 experiment. Solid dots indicate vertical-component sensors and open circles mark three-component sensors. (a) Array D with radius of 200 m deployed near the western edge of Kilauea caldera. Vertical-component sensors along the radius D00–D44 of this array were used to compare seismograms of tremor selected for study (see Fig. 4). (b) Array E with radius of 150 m deployed in the southern sector of Kilauea caldera.

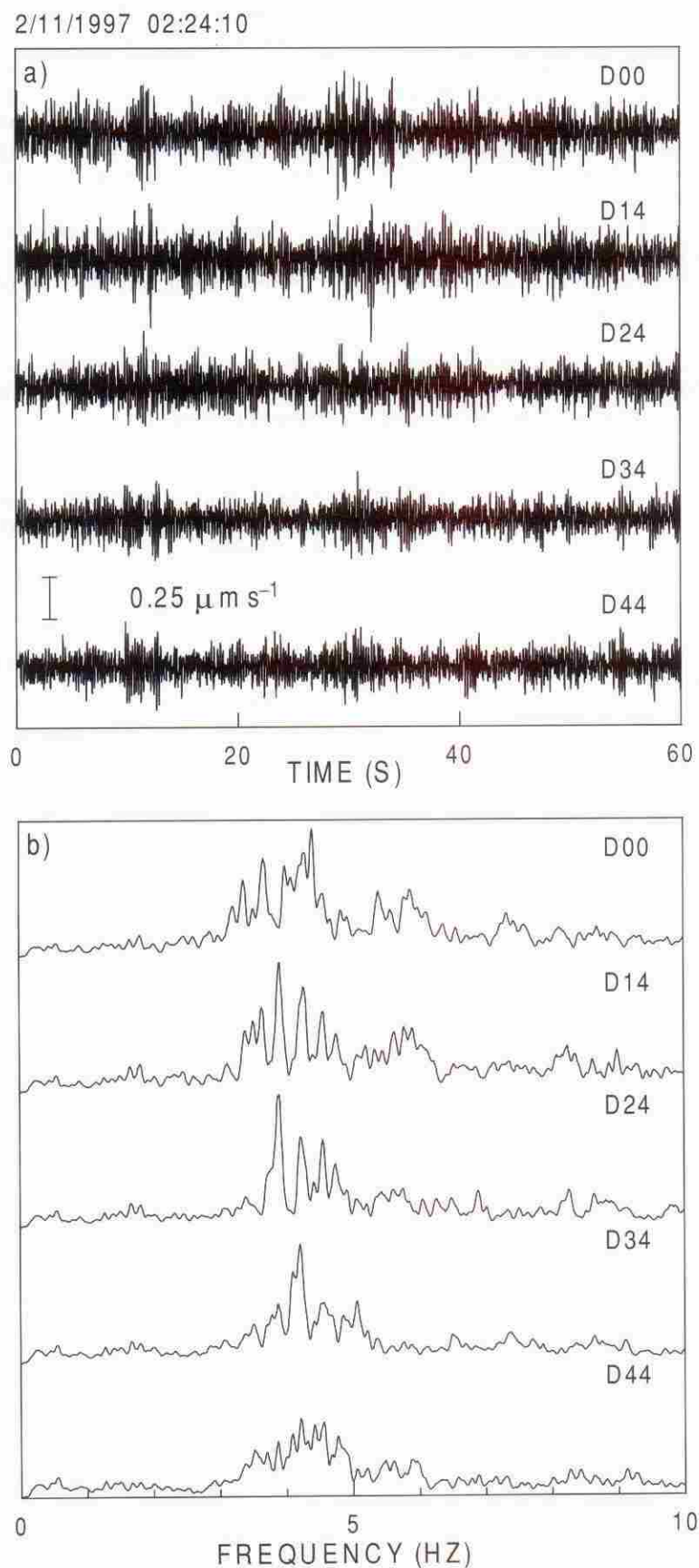


Figure 4. (a) Examples of seismograms of tremor recorded on vertical-component sensors along line D00–D44 of array D (see Fig. 3a). Sensor offset is 50 m. Date and time at the start of the record are shown at the upper left-hand side of the panel. (b) Amplitude spectra of the seismograms shown in (a). Spectral estimates have been smoothed using a 0.2 Hz wide moving window.

receivers measured counterclockwise from the direction of the x -axis.

For a single-mode 2-D wave filtered through a narrow-band filter centred at the frequency ω_0 , Aki (1957) obtained the correlation coefficient in eq. (1) in the form

$$\rho(r, \varphi, \omega_0) = \cos \left[\frac{\omega_0}{c(\omega_0)} r \cos(\theta - \varphi) \right], \quad (2)$$

where θ and $c(\omega_0)$ represent the propagation azimuth and phase velocity of the wave, respectively.

This relation shows that ρ is constant along the wave front ($\varphi = \theta \pm \pi/2$) and decays most rapidly with increasing frequency along the wave propagation direction ($\varphi = \theta$). Should a dominant wave propagation direction be present in the data, this direction may be identified in the contour map of the correlation coefficient as a function of azimuth φ and frequency ω_0 .

For an array of receivers set up along a semi-circle around a reference receiver, one obtains the azimuthal average of the correlation coefficients in eq. (2) as

$$\bar{\rho}(r, \omega_0) = J_0 \left[\frac{\omega_0}{c(\omega_0)} r \right]. \quad (3)$$

This equation shows that the phase velocity $c(\omega_0)$ of the waves can be derived by matching the Bessel function J_0 to the azimuthal average of the autocorrelation coefficients calculated for a series of receivers set in a circular pattern around a central reference receiver. Repeating the procedure as a function of frequency ω_0 yields the dispersion characteristics of $c(\omega_0)$. This equation is used for Rayleigh waves recorded on the vertical components of motion. Accordingly, we substitute $c(\omega_0)$ by $c_R(\omega_0)$ and $\bar{\rho}$ by $\bar{\rho}_z$ in eq. (3), where $c_R(\omega_0)$ represents the phase velocity of Rayleigh waves measured at the frequency ω_0 and the subscript z in the correlation coefficient refers to the vertical component of motion.

Polarized waves recorded on the horizontal components of motion are described in a similar way. Spatial autocorrelation functions $\rho_r(r, \varphi)$ and $\rho_a(r, \varphi)$ are defined as in eq. (1) for radial and azimuthal components. Radial and azimuthal components are defined here as parallel and normal, respectively, to the radii extending from the hub receiver to individual receivers on the periphery of the semi-circular array. Azimuthally averaged correlation coefficients, $\bar{\rho}_r(r, \omega_0)$ and $\bar{\rho}_a(r, \omega_0)$ are derived in the same manner as $\bar{\rho}_z(r, \omega_0)$. For a wavefield composed of a superposition of fundamental-mode Rayleigh and Love waves, and assuming that the contributions from these waves are statistically independent, we may write the correlation coefficients as (Métaxian *et al.* 1997)

$$\begin{aligned} \bar{\rho}_r(r, \omega_0) &= \alpha \left\{ J_0 \left[\frac{\omega_0}{c_R(\omega_0)} r \right] - J_2 \left[\frac{\omega_0}{c_R(\omega_0)} r \right] \right\} \\ &\quad + (1 - \alpha) \left\{ J_0 \left[\frac{\omega_0}{c_L(\omega_0)} r \right] + J_2 \left[\frac{\omega_0}{c_L(\omega_0)} r \right] \right\}, \\ \bar{\rho}_a(r, \omega_0) &= \alpha \left\{ J_0 \left[\frac{\omega_0}{c_R(\omega_0)} r \right] + J_2 \left[\frac{\omega_0}{c_R(\omega_0)} r \right] \right\} \\ &\quad + (1 - \alpha) \left\{ J_0 \left[\frac{\omega_0}{c_L(\omega_0)} r \right] - J_2 \left[\frac{\omega_0}{c_L(\omega_0)} r \right] \right\}, \end{aligned} \quad (4)$$

where α represents the contribution of Rayleigh waves to the wavefield power ($0 \leq \alpha \leq 1$), and $c_R(\omega_0)$ and $c_L(\omega_0)$ are the phase velocities of Rayleigh and Love waves, respectively. Chouet *et al.* (1998) used similar expressions based on the zeroth- and first-order Bessel functions. A recent modification of eq. (3) by Bettig *et al.* (2001), also allows an application of Aki's method to data from arrays with stations that are not equally spaced.

Aki (1957) considered two special cases. The first case represents a situation in which the wavefield power is independent of the propagation azimuth θ , and the second represents a situation in which the power of the wavefield is zero except for $\theta = \theta_0$ and $\theta_0 \pm \pi$. The former case represents an 'isotropic wave', and the latter a 'plane wave'. Aki demonstrated that for the isotropic wave the correlation coefficients $\bar{\rho}_z(r, \omega_0)$ may be replaced by the corresponding $\rho_z(r, \omega_0, \varphi)$ for arbitrary φ so that there is no need to take the average of $\rho_z(r, \omega_0, \varphi)$ with respect to φ . For a plane wave one may use either eq. (3) or simply sample the wavefield at two different azimuths. The phase velocity and propagation direction of the wave may then be obtained from eq. (2) for the vertical component of motion, or from similar relations derived for the horizontal components of motion (see eq. 50 in Aki 1957).

DATA ANALYSIS

We start with a description of the general characteristics of the wavefields inferred from the spatial patterns of the correlation coefficients versus azimuth and frequency, and follow with a presentation of the inversion procedure used to estimate the phase velocities of Rayleigh and Love waves from the spatial correlation functions obtained at each array site.

The first step in our analysis of tremor data is to determine the optimal size of the window used in the computation of the correlation coefficients. By comparing results obtained over windows of increasing lengths, we observe that the correlation coefficients calculated in the 0.5–10 Hz frequency band become stable for windows longer than approximately 2 min. We therefore select a window size of 3 min for all our calculations. Data from the A and B arrays are analysed over nine 3 min long windows, and data from the D and E arrays are analysed over six 3 min long windows.

We first bandpass filter the signal at frequency ω_0 . This is achieved by taking a discrete Fourier transform of the seismograms, windowing the spectrum with a zero-phase-shift squared-cosine (Hann) filter with a fixed bandwidth of 0.5 Hz, and transforming the result back to the time domain. The correlation coefficients are then derived for individual azimuths by multiplying the filtered signals obtained on receiver pairs using the hub as a reference station. Results are obtained for individual frequencies stepped in increments of 0.25 Hz spanning the bandwidth 0.5–10 Hz. When treating horizontal components in the semi-circular arrays, the outer ring components are rotated in the radial and transverse directions to the hub, and the hub components are rotated parallel to each of the outer ring components, before proceeding with the filtering and multiplication operations.

Fig. 5 shows colour maps of the correlation coefficients $\rho(r, \varphi, \omega_0)$ versus azimuth and frequency obtained for a receiver spacing $r = 100$ m in array A. No obvious predominant direction of wave propagation is observed in the vertical component of motion, suggesting that this component of the wavefield is composed of equal contributions from waves scattered by sources distributed over the entire azimuthal range. In contrast, the shapes of the colour patterns for radial and transverse components at frequencies below 4 Hz are elongated in the E10°N–W10°S direction, suggesting a predominant wave propagation azimuth close to N10°W or S10°E. This finding is consistent with independent measurements of wave propagation azimuths based on frequency-slowness analyses of the same data (Saccorotti *et al.* 2001b).

Fig. 6 shows similar colour maps obtained for array D. Again, no preferential directions of propagation are observed in the data

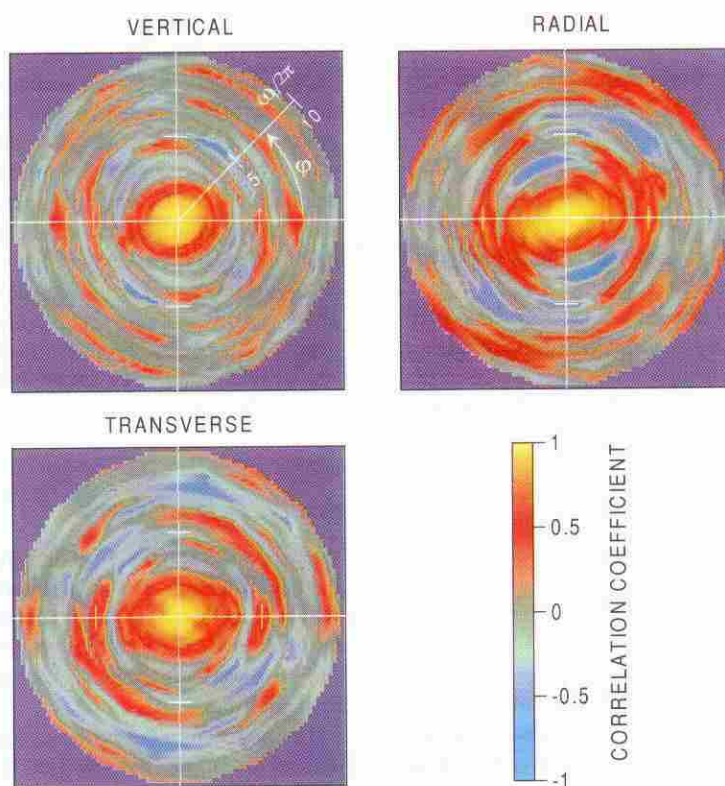


Figure 5. Colour maps of the correlation coefficients $\rho(r, \varphi, \omega_0)$ obtained as functions of bandpass filter frequency and azimuth for a receiver spacing $r = 100$ m in array A. The three plots represent the vertical, radial, and transverse components of ground velocity. The maps are represented in polar coordinates in which the angle is the azimuth and the frequency axis runs along the radius of the circular map with the origin at the centre and outermost circle corresponding to 10 Hz. Tick marks are 5 Hz marks. The vertical and horizontal axes are oriented N–S and E–W, respectively. The main diameter of the array is oriented E17°N and the top half of each map is obtained from the bottom half by symmetry.

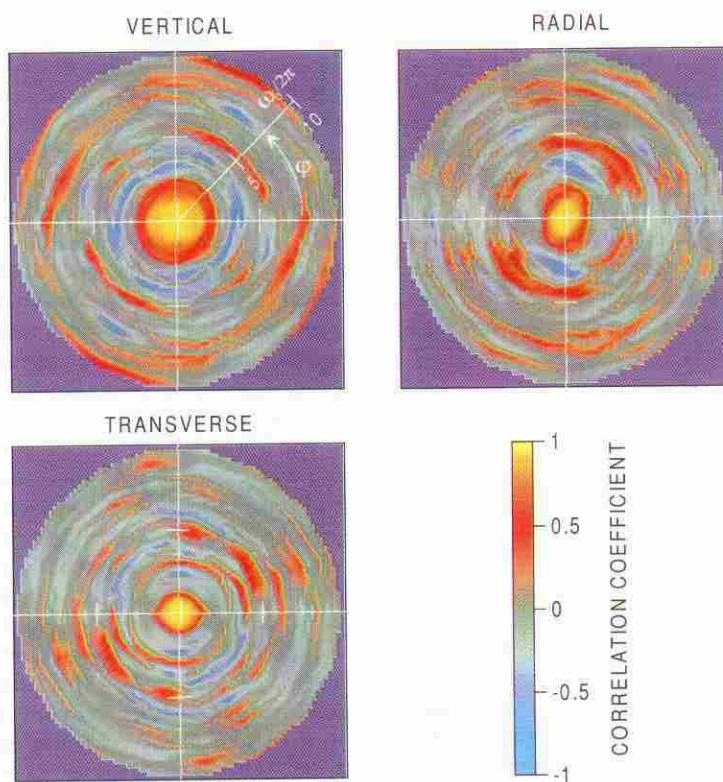


Figure 6. The same as Fig. 5 for array D. The main diameter of the array is oriented N30°W and the right half of each map is obtained from the left half by symmetry.

from this array except for wave components at frequencies below 2 Hz on the radial component, which point to a dominance of waves propagating in the E20°S–W20°N direction.

To determine the composition and phase velocities of the waves composing the wavefield, we calculate azimuthal averages of the correlation coefficients within each frequency band for each component of motion. We then fit eqs (3) and (4) to these data by performing a grid search aimed at minimizing the norm function

$$\|\mathbf{d} - \mathbf{G}(\mathbf{m})\|^2, \quad (5)$$

where \mathbf{d} is the data vector containing the correlation coefficients, \mathbf{m} is the vector of model parameters containing the phase velocities of Rayleigh and Love waves and the unknown parameter α in eq. (4) and \mathbf{G} represents a non-linear forward modelling operator relating data to model parameters. The latter operator is represented by either eq. (3) or (4) depending on the component of motion considered. The solution of eq. (5) is simplified through the definition of $c(\omega_0)$ as a continuous function of frequency (e.g. Métaxian *et al.* 1997; Chouet *et al.* 1998; Bettig *et al.* 2001). To determine which functional relationship is more adequate for describing the dispersion characteristics of our wavefields, we first obtain spot estimates of the phase velocities from readings of zero-crossings, maxima and minima (Aki 1957; Chouet *et al.* 1998) in the correlation functions calculated for array D. Based on our inspection of these data (see Figs 13e and f, below), we select *a priori* models of wave dispersion characteristics in the form (Ferrazzini *et al.* 1991; Métaxian *et al.* 1997)

$$c(f) = Af^{-b}, \quad (6)$$

where c is the phase velocity, f is the frequency, and A and b are constants. Different coefficients A and b are used to model Rayleigh and Love waves, and in the following we use the subscripts R and L to refer to Rayleigh and Love waves, respectively.

At each array site, our inversion procedure consists in a search for the set of coefficients A_R and b_R in the vertical-component arrays, and the set of coefficients A_R , b_R , A_L , b_L and α in the three-component arrays, for which the squared sum of residuals between the observed and predicted correlation curves is minimized. The coefficients A and b are sought over a grid of discrete values spanning the range 0.1–4, and α is sought over a grid of discrete values spanning the range 0–1, using a grid spacing of 0.02.

Note that eqs (3) and (4) provide two independent estimates of $c_R(\omega)$, and for a 3-D array three separate inversions can be performed. One approach consists in performing two separate inversions for the vertical and horizontal components. In that case the forward modelling operator in eq. (5) is represented by eq. (3) or eqs (4), yielding two independent estimates of $c_R(\omega)$. Another approach consists in a simultaneous inversion of the correlation data obtained from the three components of motion. In that case, we perform a single search in the model parameter space and substitute the forward modelling operator \mathbf{G} in eq. (5) by eq. (3) or (4) depending on the component of motion being considered. A third approach consists in an estimation of $c_R(\omega)$ from an inversion of the correlation data obtained for vertical components, and substitution of the dispersion characteristic derived in that manner into the arguments of eq. (4). This approach has the obvious advantage that the number of unknowns in the horizontal components is reduced to the three coefficients A_L , b_L and α . Our tests indicate that the first method produces unrealistically high velocities of Rayleigh waves at frequencies above 5 Hz, while the latter two approaches yield very similar results, with the previous method showing slightly lower rms inversion residuals.

Accordingly, we adopt this third method to invert our correlation data. The results of these inversions are described below.

Fig. 7 shows the azimuthally averaged correlation coefficients calculated for the nine data windows for receiver spacings of 50, 100 and 150 m in array A. The striking similarities among the correlation data derived from distinct time windows lend strong support to our assumption of a stationary stochastic wavefield. The smooth curves superimposed on the data represent fits of eqs (3) and (4) to the experimental correlation data.

Results for arrays D and E are shown in Figs 8 and 9, respectively. As in Fig. 7, the smooth curves superimposed on the data are obtained from fits of eqs (3) and (4) to the experimental correlation data. In the fits displayed in Figs 7–9, the arguments of the Bessel functions are fixed by dispersion curves, the shapes of which are given by eq. (6). The parameters A , b and α are obtained by solving eq. (5) and are listed in Table 1 for each array.

The values estimated for the parameter α indicate that the partitioning of energy among Rayleigh and Love wave modes is similar at arrays A and D, once the uncertainties in these estimates are taken into account.

Overall, the experimental data are fitted reasonably well by the theoretical functions, supporting our assumption of a stochastic wavefield dominated by dispersive surface waves. At array A, poor fits are observed on the transverse component at a receiver spacing of 100 m, and on the vertical and radial components at receiver spacing of 150 m (Fig. 7), where significant differences are noted between the fitting function and the experimental data at frequencies near 5 Hz. This discrepancy may be related to the presence of narrow-band waves that are significantly faster than those observed at neighbouring frequencies. Frequency-slowness analyses by Saccorotti *et al.* (2001b) indeed suggest that the 3–5 Hz tremor wavefield includes bursts of non-dispersive waves propagating with apparent velocities near 2 km s⁻¹ (see, for example, fig. 7 in Saccorotti *et al.* 2001b).

To test this interpretation, we calculate theoretical Bessel functions for narrow-band non-dispersive body waves superimposed on a wide-band wavefield dominated by surface waves. In this case, we obtain the correlation coefficient in the form

$$\bar{\rho}_{\text{tot}}(r, \omega_0) = [1 - w(\omega_0)]\bar{\rho}_d(r, \omega_0) + w(\omega_0)\bar{\rho}_{\text{nd}}(r, \omega_0), \quad (7)$$

where $\bar{\rho}_{\text{tot}}(r, \omega_0)$ represents the total correlation coefficient, $\bar{\rho}_d(r, \omega_0)$ and $\bar{\rho}_{\text{nd}}(r, \omega_0)$ are the correlation coefficients representing the dispersive and non-dispersive components of the wavefield, respectively, and $w(\omega_0)$ is a weight function expressing the relative contribution of the non-dispersive components to the wavefield. The function $w(\omega_0)$ describes the shape of the narrow-band power spectrum assumed for the body waves. We assume a power spectrum centred at the frequency ω_{nd} and express $w(\omega_0)$ by the function

$$w(\omega_0) = A \exp \left[\frac{-(\omega_0 - \omega_{\text{nd}})^2}{\sigma^2} \right], \quad (8)$$

where A ($0 < A < 1$) and σ are factors defining the amplitude and width of the spectral peak, respectively.

Using eq. (7) we replace $\bar{\rho}_d(r, \omega_0)$ by the combination of Bessel functions obtained in our earlier fits, and replace $\bar{\rho}_{\text{nd}}(r, \omega_0)$ by the correlation coefficients in eqs (3) and (4) calculated for the appropriate receiver spacing and for constant (frequency-independent) values of the phase velocities c_R and c_L . For non-dispersive waves the velocities c_R and c_L represent the apparent horizontal velocities of the *P/SV* and *SH* components of the wavefield, respectively. We assume that the relative contributions of the *P/SV* and *SH* waves to the non-dispersive wavefield power are identical to those estimated earlier for Rayleigh and Love waves (see Table 1). Using a

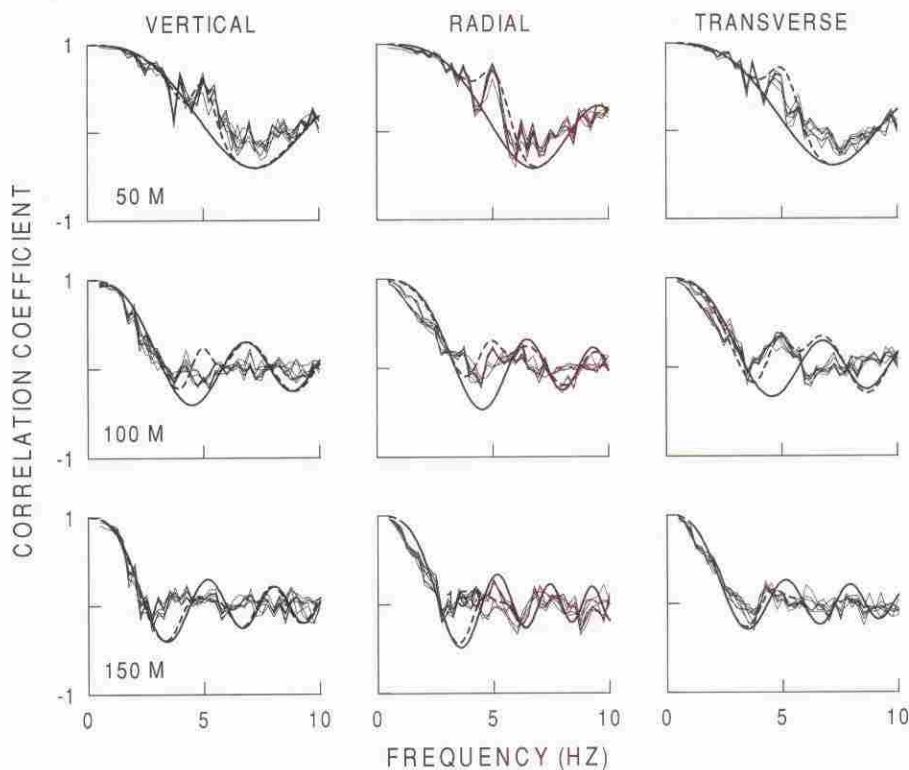


Figure 7. Azimuthally averaged correlation coefficients (thin lines) obtained as a function of bandpass filter frequency for the vertical, radial, and transverse components of motion in array A for the nine data windows analysed. From top to bottom, the plots show results obtained for receiver spacings of 50, 100 and 150 m. The bold lines superimposed on the correlation data are the theoretical correlation coefficients derived by fitting eqs (3) and (4) to the data. The dashed lines show theoretical correlation coefficients obtained under the assumption that the wavefield is composed of a superposition of wide-band dispersive waves and narrow-band non-dispersive waves (see eqs 7 and 8 in the text).

trial-and-error procedure we obtain a reasonable fit to the observed correlation coefficients for the parameters $c_R = c_L = 2 \text{ km s}^{-1}$, $A = 0.8$, $\sigma = 0.89 \text{ s}^{-1}$ and $\omega_{nd} = 31.41 \text{ s}^{-1}$. The results are illustrated by the dashed curves in Fig. 7.

However, the misfit discussed above cannot be solely attributed to the presence of body waves radiated from the primary source. Independent frequency-slowness analyses of tremor recorded on array A (Saccorotti *et al.* 2001b) and array E (Almendros *et al.* 2001) suggest that the source of tremor may have changed significantly between 1996 and 1997. Measurements by Almendros *et al.* (2001) (see fig. 7b in Almendros *et al.* 2001) point to a dominance of waves with velocities of $0.7\text{--}1.4 \text{ km s}^{-1}$ at array E. These velocities are significantly lower than the velocities near 2 km s^{-1} inferred by Saccorotti *et al.* (2001b) for the P - SV and SH components of motion at array A. Although the epicentral source region appears to have remained stationary between 1996 and 1997, the hypocentral region might have been slightly shallower in 1997 compared with 1996. We note, however, that the azimuthally averaged correlation coefficients obtained for vertical components are quite similar in arrays A (Fig. 7) and E (Fig. 9), suggesting that a source effect is an unlikely explanation for the origin of the body waves discussed above. A better interpretation of the origin of these fast narrow-band waves might be a path and/or site effect independent of the details of source radiation. Arrays A and E were essentially co-located on a ponded pahoehoe flow that filled a shallow depression near the southern caldera boundary. The flow has a thickness of 10–20 m and probably corresponds to the 17 m thick layer composing the top layer in our velocity model (see below). This layer is underlain by a layer with a shear wave velocity that is twice as high as that of

the surficial layer. The shallow pahoehoe-filled basin may thus have acted as an efficient trap for body waves impinging the basin with steep incidence angles. Based on this interpretation, the anomaly common to both the 1996 and 1997 data would simply reflect the particular structural setting beneath arrays A and E.

We use the horizontal-to-vertical (H/V) spectral ratio method (Nakamura 1989; Mora *et al.* 2001) to investigate the site response beneath array A and test the reliability of the latter assumption. Mean spectral ratio calculated at receivers of the intermediate ring and hub receiver in array A, are displayed in Fig. 10. The H/V spectral ratio shows a sharp peak near 5 Hz, in harmony with our assumption of a site effect being the underlying cause of the misfit observed at array A. While attractive, this idea nevertheless needs further quantitative testing to fully assess its validity. Such tests, however, require detailed simulations of wave propagation in 3-D heterogeneous media, and are left for future studies.

The colour maps of correlation coefficients versus azimuth and frequency obtained at array A (Fig. 5) indicate that the vertical component wavefield is dominated by waves for which the propagation directions are distributed almost isotropically over the entire azimuthal range. This observation suggests that eq. (3) can also be used to interpret the correlation measurements made at fixed azimuth ϕ in the linear array B. In the following, the data from array B are analysed over the same window length and frequency bands as those selected in our previous treatment of data from the semi-circular arrays. To take full advantage of the spatial extent of the linear array, we consider data from consecutive overlapping subarrays, each composed of five stations, and calculate the frequency-dependent correlation coefficients for all the independent combinations of station pairs in

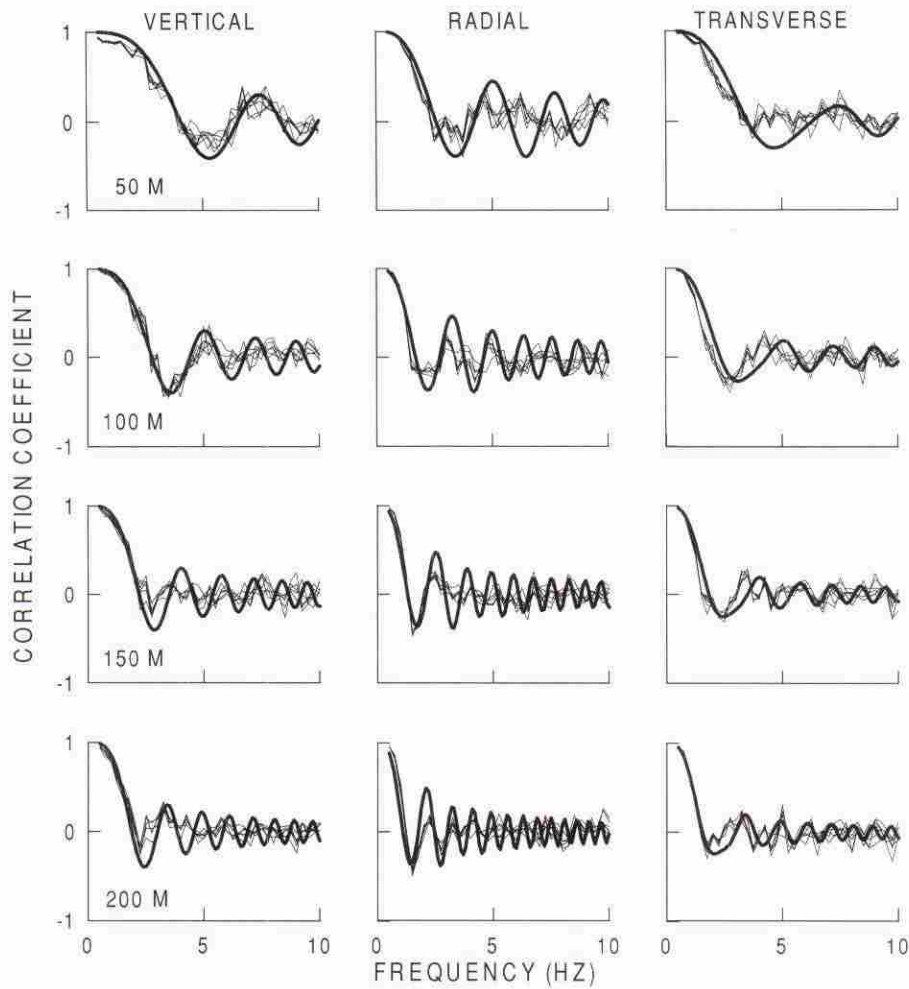


Figure 8. The same as Fig. 7 for the three components of motion recorded in array D. From top to bottom, the plots show results obtained for receiver spacings of 50, 100, 150 and 200 m.

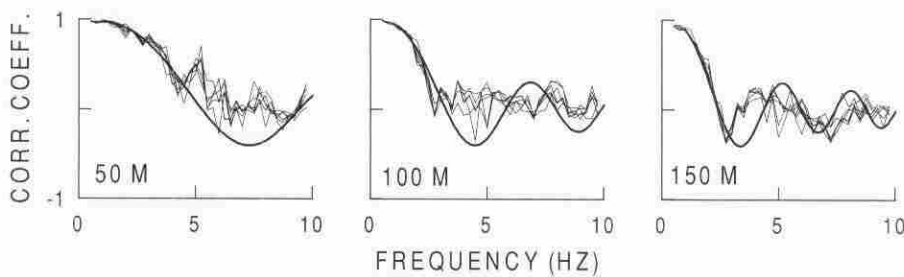


Figure 9. The same as Fig. 7 for the vertical component of motion recorded in array E. From left to right, the plots show results obtained for receiver spacings of 50, 100 and 150 m.

Table 1. Dispersion characteristics of surface waves recorded on arrays A, D and E.

Array	A_R	b_R	A_L	b_L	α
A	$1.40^{+0.58}_{-0.40}$	$0.44^{+0.26}_{-0.18}$	$2.42^{+1.55}_{-0.90}$	$0.76^{+0.34}_{-0.49}$	0.45 ± 0.10
D	$1.60^{+0.34}_{-0.24}$	$0.78^{+0.10}_{-0.10}$	$0.62^{+0.26}_{-0.14}$	$0.60^{+0.48}_{-0.32}$	0.30 ± 0.15
E	$1.38^{+0.60}_{-0.38}$	$0.42^{+0.44}_{-0.20}$	—	—	—

each subarray. This procedure allows estimations of the correlation coefficients over receiver spacings ranging between 35 and 140 m. We select a subarray overlap of four receivers. Calculations are iterated separately for receivers B01–B20, and receivers B21–B48.

In the following, we refer to these two segments as the NW and SE segments, respectively. This choice of segmentation is motivated by our observation that significant waveform changes occur across the morphological discontinuity associated with the southern caldera boundary located between receivers B20 and B21 (Saccorotti *et al.* 2001b) see also figs 1 and 2). Correlation data obtained at individual subarrays are then complemented by the spatial correlation coefficients calculated at frequencies of 0.5, 0.75, 1 and 1.25 Hz for all the receiver spacings available along the two profiles. This allows us to put further constraints on the average velocity distributions at longer wavelengths beneath the two linear segments. Using the procedure described earlier, these data are inverted to obtain the dispersion

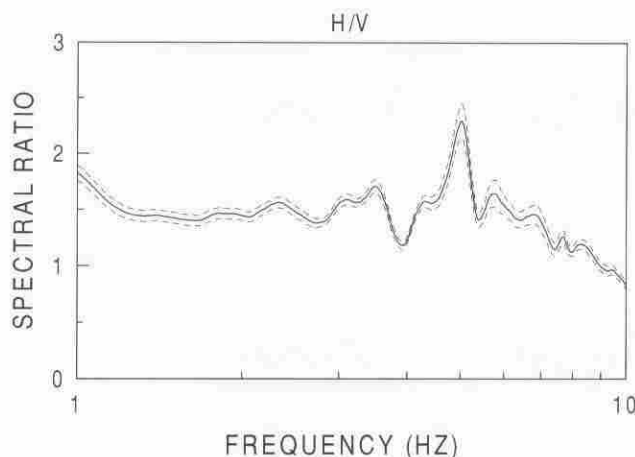


Figure 10. Mean horizontal-to-vertical spectral ratios (continuous line) and variance $\pm 1\sigma$ of the mean (dashed lines) for receivers in array A. The spectral ratios are obtained by first calculating Fourier spectra for seven 80 s long windows in the data from receivers of the intermediate ring and hub receiver in array A. Horizontal-component spectra are then estimated by taking the geometric average of the spectra of the radial and transverse components of motion. Finally, the resulting spectra are smoothed using a 0.2 Hz-wide moving window, and a mean spectral ratio is obtained as the logarithmic average of individual ratios calculated for the different time windows and array receivers.

characteristics of Rayleigh waves along the B-line. The correlation curves and Bessel fits obtained for subarray B08–B12 are shown in Fig. 11(a), and the correlation curves obtained as a function of distance for the four frequencies are shown in Fig. 11(b).

DISPERSION FUNCTIONS AND VELOCITY STRUCTURES

The coefficients in Table 1 describe the dispersive characteristics of surface waves observed at each array site. These coefficients are derived from the minima of the norm function (5). To fix error bounds in these estimates, we need to bound the region of the norm function that contains models for which the fits to the data are equally good within some confidence limit. This is achieved by calculating the ratios of the variances of individual models to the variance of the model showing the minimum misfit, and selecting models for which the variance ratios are lower than or equal to the 95 per cent limit of the inverse cumulative F -distribution calculated for the appropriate number of independent data samples and model parameters (Menke 1989, p. 96; Del Pezzo *et al.* 2001).

An example of the results obtained with this error estimation procedure is shown in Fig. 12 for the vertical-component data from array A. The first step in our procedure is a calculation of the norm function (5), and normalization of the results using the minimum value. To identify models within the region corresponding to the 95 per cent confidence limit, we need to know the number of degrees of freedom in our estimate of the norm function. This number is equal to the number of independent data samples minus the number of model parameters. In the vertical-component array A, the number of independent data samples used in the inversion is equal to the number of correlation coefficients obtained in individual frequency bands (39), times the number of independent data windows analysed (9), times the number of interreceiver distances considered (3). This yields 1053 independent data samples. To this quantity we subtract the number of model parameters, which equals 2 in the inversion of

vertical-component data for Rayleigh wave dispersion. The 95 per cent confidence limit in the estimates of the A_R and b_R coefficients obtained from the discretized values of the norm function (5) is thus given by the inverse cumulative F -distribution of the ratio of two random variables, each having 1051 degrees of freedom. This yields a value of 1.107. Models associated with values of the normalized norm function that are lower than or equal to 1.107 are therefore considered to yield equivalent fits to the data with a probability of 95 per cent (Fig. 12).

Within each individual frequency band, we use this set of equivalent models to retrieve the lower and higher values of phase velocity. This procedure provides extreme dispersion curves that represent the 95 per cent error limits on the dispersion function defined through the minimum misfit coefficients A_R and b_R . The same procedure is applied to horizontal-component arrays, in which we use misfit functions derived by substituting the lower and upper bounds of Rayleigh waves dispersion characteristics into eq. (4). This yields uncertainties in the A_L , b_L and α coefficients that include the errors associated with the estimates of A_R and b_R . The errors calculated in that manner are listed in Table 1 along with the A , b and α coefficients defining the dispersion functions.

Structural models consistent with the dispersion characteristics obtained at individual array sites may be derived under the assumption that those dispersions represent the fundamental modes of Love and Rayleigh waves. Using Herrmann's code (Herrmann 1987), we follow a trial-and-error procedure in our search for structural models that produce phase velocities compatible with the experimental dispersions. We begin our analysis with data from array A and first consider a simple model consisting of a single layer underlain by a homogeneous half-space. The velocities in the layer and half-space, and layer thickness, are adjusted to fit the low- and high-frequency limits in the distribution of experimental data. We then fit the curvature of the dispersion data by gradually increasing the number of layers in the model. Layer thicknesses and velocities are modified until a satisfactory fit is obtained. This structure is used as a starting model in the inversion procedure, which is iterated until the rms between the observed and predicted dispersion curves is smaller than 0.01. Once the velocity structure beneath array A is known, the same structure is used as a starting model in the inversions of dispersion data at the D, E and B01–B05 arrays.

Figs 13(a) and (b), respectively, show the dispersion characteristics of Rayleigh and Love waves, together with their error bounds, measured in the 0.5–10 Hz band at array A. Fig. 13(c) displays the dispersion characteristics for Rayleigh waves at array E. The corresponding shear wave velocity structure is shown in Fig. 13(d), together with data (grey strips) obtained by Dawson *et al.* (1999) from a high-resolution (0.5 km resolution) tomographic inversion of arrival times from local earthquakes.

Rayleigh wave dispersion characteristics obtained at arrays A and E are very similar, which is not surprising in view of the fact that the two antennas were essentially co-located. The dispersion characteristics of Love waves obtained at array A include large uncertainties, a direct consequence of the poor Bessel fits obtained for horizontal components in that array. Accordingly, we made no attempt to use these Love wave dispersion data in our search for a velocity model. Rather, our velocity model is obtained by inverting the combined Rayleigh wave dispersion data from arrays A and E.

The dispersion curves of Rayleigh and Love waves obtained at array D, and the corresponding velocity model, are shown in Figs 13(e)–(g), respectively. Here also, our structural model is obtained from an inversion of Rayleigh wave dispersion data alone. Rayleigh and Love wave dispersion data at this site are markedly

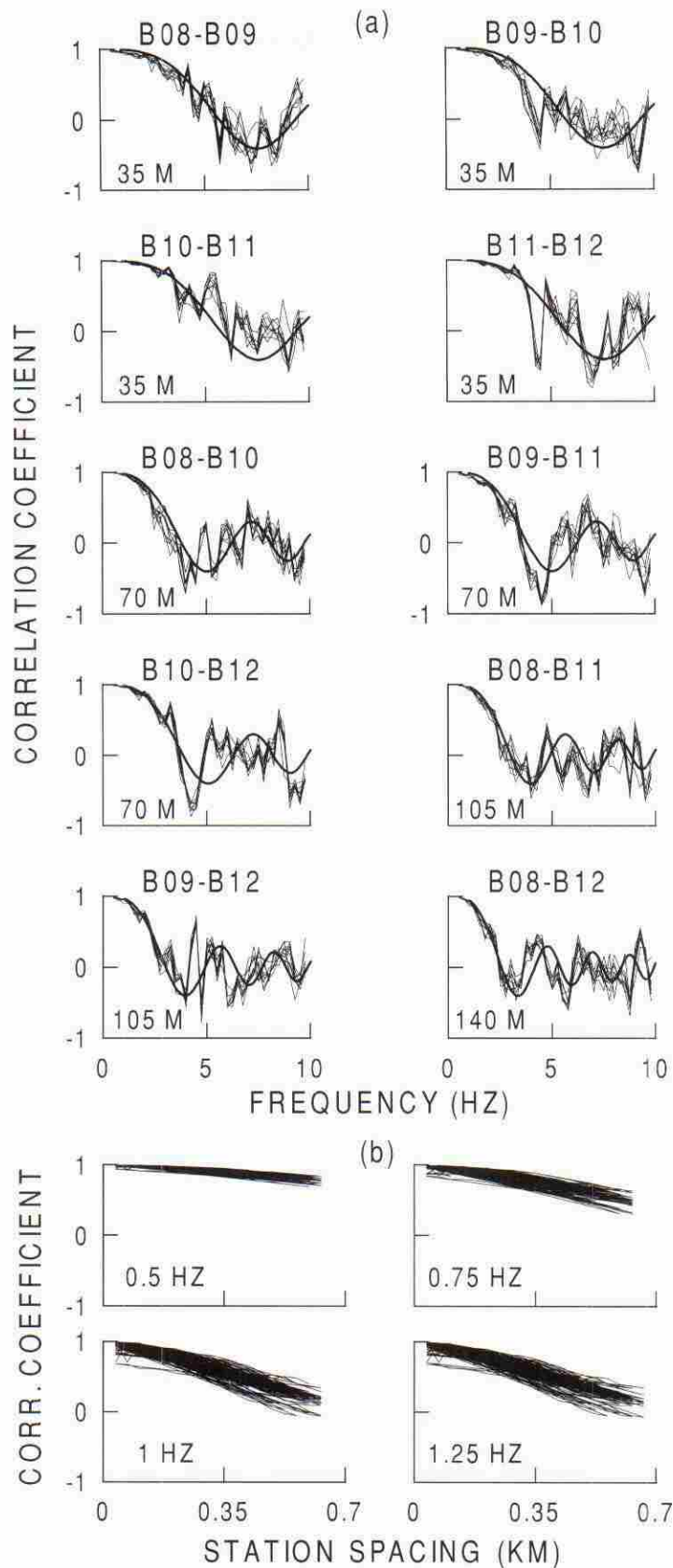


Figure 11. (a) Correlation coefficients (thin lines) obtained as a function of bandpass filter frequency for stations B08–B12 in linear array B for the nine data windows analysed. From left to right and from top to bottom, the plots show the results obtained for receiver spacings of 35 m (first four plots), 70 m (next three plots), 105 m (next two plots) and 140 m (last plot at the bottom right). The bold lines superimposed on the data are the theoretical correlation coefficients derived by fitting eq. (3) to the data. (b) Correlation coefficients derived at a fixed frequency for increasing receiver spacing. These data have been added to those in (a) when evaluating the theoretical correlation functions in eq. (3).

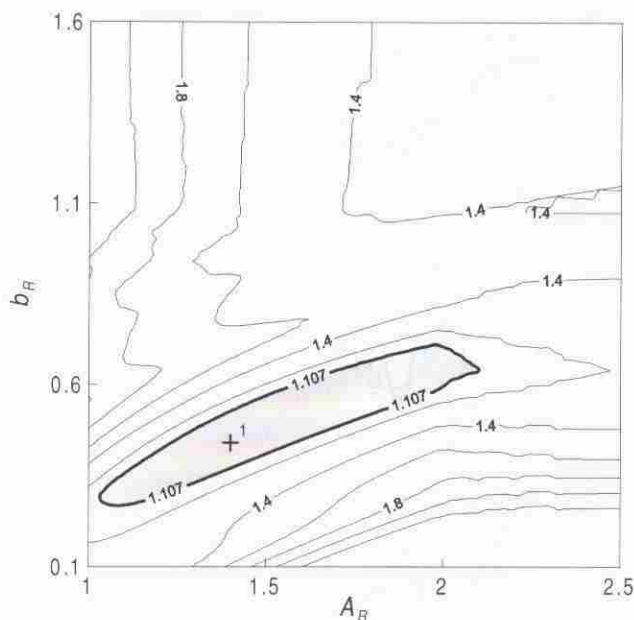


Figure 12. Contour plot of the residuals associated with the solution of the norm function (5) for data from the vertical-component array A. The data are normalized to their minimum. The shaded area bounded by the bold line marks the 95 per cent confidence interval in the estimate of the A_R and b_R coefficients. The cross indicates the minimum misfit node.

different, showing Love velocities to be lower by a factor of up to 3 compared with Rayleigh velocities in the 1–5 Hz frequency range (Figs 13e and f). Such results may be interpreted in terms of a higher density of vertical versus horizontal cracks at site D compared with site A, resulting in lower shear moduli controlling *SH* wave speeds compared with those controlling *SV* wave speeds at the former location (Aki *et al.* 1978).

At each array site, we found that a five-layer model was adequate to satisfactorily fit the observed phase velocities. We kept the layer densities and Poisson ratios fixed in all our inversions, and inverted the observed dispersion characteristics for shear wave velocities alone. This is reasonable as Rayleigh wave velocities depend strongly on the shear velocity structure, and weakly on density and Poisson ratio (Xia *et al.* 1999; Louie 2001). Our shear wave velocity models are obtained with a constant Poisson ratio $\nu = 0.33$ corresponding to $V_p/V_s = 2$, a value appropriate for the shallow-velocity structure beneath the Kilauea caldera (Dawson *et al.* 1999). Density profiles are derived from the compressional velocities according to the relation (Gardner *et al.* 1974)

$$\rho = 0.23 V_p^{1/4}, \quad (9)$$

where V_p is in units of m s^{-1} and ρ is in units of g cm^{-3} . A simple method to estimate error bounds in the velocity structures is to fit models to the high and low confidence limits of the dispersion curves (Chouet *et al.* 1998; Louie 2001). This procedure yields velocity profiles corresponding to the velocity bounds allowed by

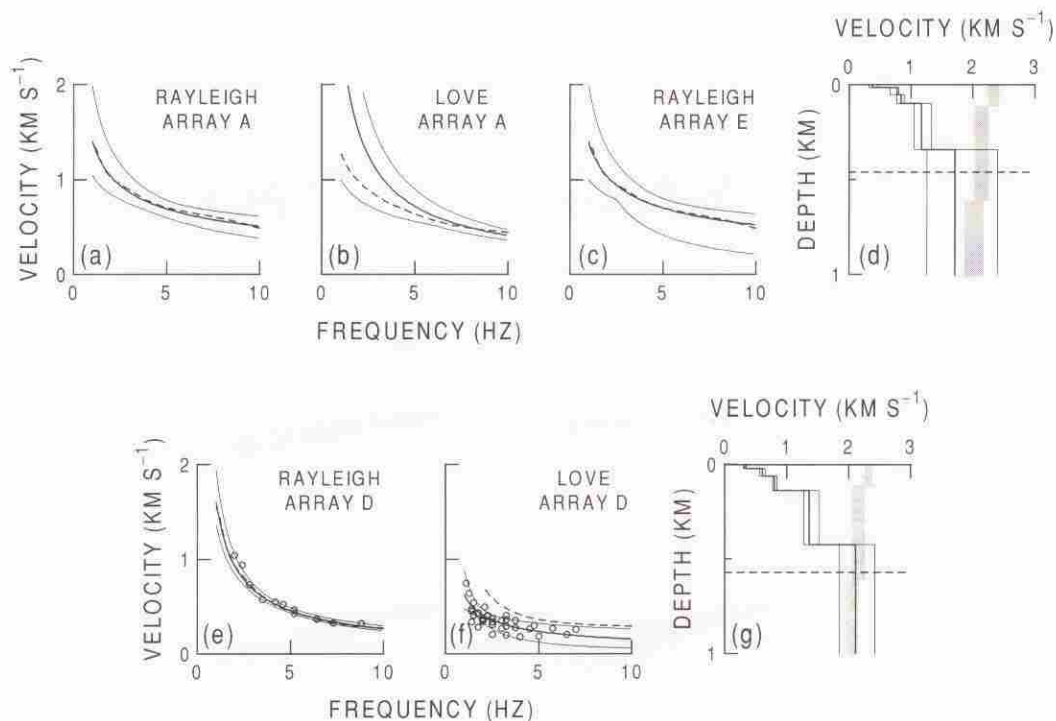


Figure 13. Dispersion curves for (a) Rayleigh and (b) Love waves obtained from fits of eqs (3) and (4) to the azimuthally averaged correlation coefficients calculated within the 0.5–10 Hz frequency band at array A. Bold lines are the dispersion functions obtained from the fits, and thin lines represent the 95 per cent confidence limits on these fits. Dashed lines represent the dispersion functions predicted from the shear wave velocity structure depicted in (d). (c) The same as in (a), but for array E. (d) Shear wave velocity model derived from inversion of the experimental Rayleigh wave dispersion characteristics obtained at arrays A and E. The bold line represents the best velocity model, and thin lines are extreme velocity models derived from inversions of the error bounds in the dispersion functions. The grey strips represent velocities obtained by Dawson *et al.* (1999) from traveltime tomography. The dispersion curves for Rayleigh and Love waves, and corresponding velocity model for array D are shown in panels (e)–(g), respectively. Open circles in panels (e) and (f) represent phase velocities obtained from zero-crossings, maxima, and minima of the correlation functions versus distance and frequency. The dashed lines in the velocity models of panels (d) and (g) mark the depth resolution limits in the velocity inversion procedure as defined in Herrmann (1987).

the dispersion curves. To avoid unrealistically high velocities in the deeper parts of the model resulting from the steep slopes of the dispersion curves predicted by eq. (6) at low frequencies, we used a lower-frequency limit of 1 Hz in our inversion of the dispersion relationships.

Including error bounds, the velocities below array D are generally comparable to those obtained under arrays A and E. The velocity structures obtained at both sites include two surficial low-velocity layers with cumulative thicknesses of 50–60 m and shear wave velocities of 0.3–0.8 km s⁻¹. Underlying the top two layers are two thicker layers extending to depths of 340–420 m with shear wave velocities in the 0.8–1.5 km s⁻¹ range. A discrepancy is observed between the velocities obtained at depths shallower than 400 m in our models and the velocities derived by Dawson *et al.* (1999) from traveltimes tomography. The velocities obtained by Dawson *et al.* (1999) are systematically higher by 0.5–1.0 km s⁻¹ compared with our models. This discrepancy may be attributed to a lack of resolution of the tomography method in the top 500 m of the Kilauea structure, owing to the small number of very shallow earthquakes available to image this layer. The bottom half-spaces in our models all display shear wave velocities near 2 km s⁻¹, in optimum agreement with the results of traveltimes tomography.

In a previous study (Saccorotti *et al.* 2001b), we presented a preliminary velocity structure beneath arrays A and B displaying a half-space velocity roughly 15 per cent higher than the upper bound derived in the present study beneath the same site. This difference stems from two factors. First, our earlier inversion was based on data from the entire array B and was more sensitive to longer wavelengths that sample deeper (and faster) portion of crust. Secondly, at the time of this preliminary study the tomographic model of Dawson *et al.* (1999) was not yet available, so that independent constraints on the velocities of the deeper layers were lacking.

A structural model compatible with the data from linear array B is shown in Fig. 14. The topographic discontinuity marking the caldera boundary has a corresponding discontinuity in the subsurface distribution of shear velocities. There is also a gradual thickening of the low-velocity layers toward the southeast along the B-line, in harmony with the results obtained by Dawson *et al.* (1999), who observed a lowering of the compressional and shear velocities in

the first kilometre of structure along the south edge of the caldera. Dawson *et al.* (1999) attributed this observation to lower rigidities and densities of pyroclastic deposits south of the caldera, compared with the mechanical properties of accumulated prehistoric and historic pahoehoe lava flows filling the caldera interior.

The significance of the results obtained with the B array must be examined in light of the resolving capabilities of our inversion procedure. Using the error analysis method described earlier, we obtained confidence limits in the dispersion functions for the end subarrays formed by receivers B16–B20 and receivers B21–B25. Confidence limits in the velocity models were obtained from inversions of the upper and lower bounds in phase velocities measured in both subarrays. The results of our calculations, shown in Fig. 15, indicate that the resolving capabilities of our method are adequate to properly detect the reported differences in the velocity structures. This suggests that surface wave dispersion data based on array measurements of tremor may provide an economic and reliable tool for mapping the actual limits of collapsed caldera structures.

DISCUSSION AND CONCLUSION

We used Aki's correlation method (Aki 1957, 1965) to measure the phase velocities of Rayleigh and Love waves at different array sites in and around the summit caldera of the Kilauea Volcano, Hawaii. The phase velocities were then inverted to obtain models of the shallow shear wave velocity structures beneath the arrays based on the assumption that the observed dispersions are representative of fundamental-mode surface waves. An analysis of surface wave dispersion characteristics along the trace of linear array B provides quantitative evidence of a velocity contrast marking the boundary between the inner and outer caldera structures. The robustness of our results was checked by comprehensive tests of inversion uncertainties based on statistical analyses of the error functions.

Several limitations in our results need to be underlined here. First is the non-uniqueness of the velocity structures determined from inversions of the surface wave dispersion characteristics. Owing to the integrative nature of the relationships between the dispersion functions and the depth distribution of shear velocities (e.g. Herrmann

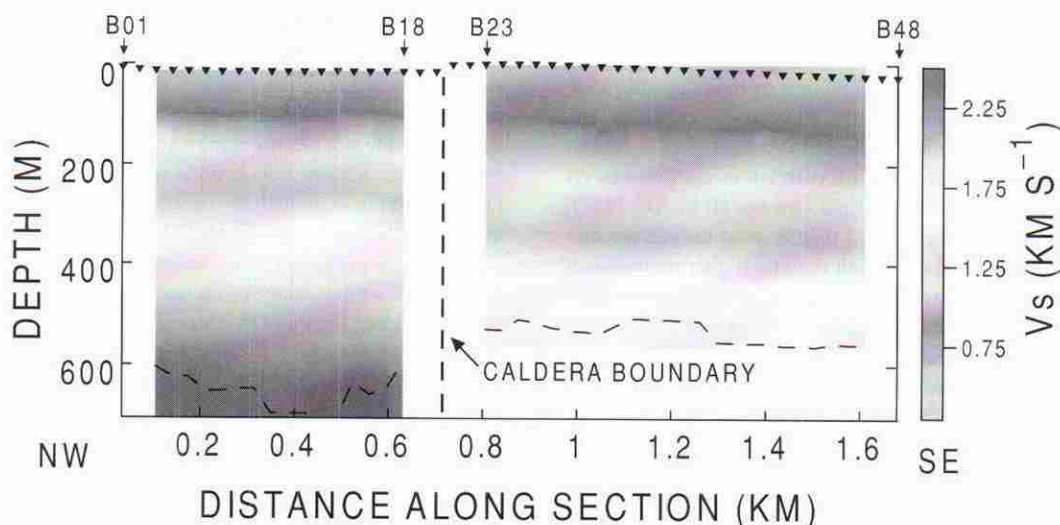


Figure 14. 2-D shear wave velocity structure along the trace of linear array B. Velocity increases from colder to warmer colours according to the scale at the right. Triangles at the top of the plot mark the locations of the receivers used in the analysis. The dashed lines mark the spatial resolution limits in the velocity inversions.

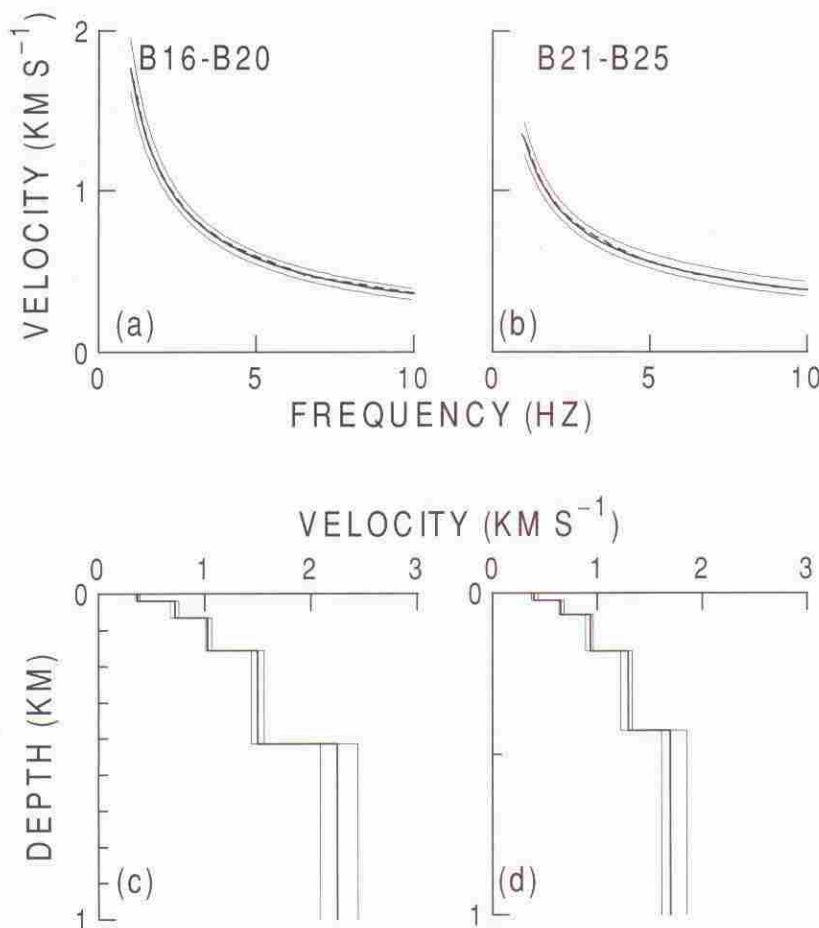


Figure 15. Resolution limits of the velocity inversion along linear array B. Dispersion curves obtained for subarrays B16–B20 (a) and B21–B25 (b). Bold lines represent the experimental dispersion curves, and dashed lines are dispersions predicted by the velocity models shown in (c) and (d), respectively. Thin lines represent error bounds in the experimental dispersion curves. Shear wave velocity structure beneath subarray B16–B20 (c) and B21–B25 (d). Bold lines indicate the best models and thin lines show the corresponding error bounds.

1987), different models can fit the data equally well. Although the velocity structures presented here are representative of the average subsurface velocity distributions, caution must be exercised when adopting these models for calculating Green functions at frequencies higher than a few Hz, and comprehensive testing using equivalent traveltime models is recommended. Secondly, our velocity inversions were performed under the assumption of fundamental-mode Rayleigh and Love waves. In principle, Aki's method could be extended to allow a determination of the phase velocities of n modes. This would require an estimation of correlation coefficients on $2n - 1$ semi-circles with different radii (see eq. 60 in Aki 1957). The array data considered here could thus be used to seek the dispersion characteristics associated with the first higher mode. Such an objective, however, requires a large number of model parameters as it involves a determination of both the velocity and partitioning of power associated with each mode for each frequency. For phase velocities, the number of unknowns can be reduced by defining $c(\omega)$ as a continuous function of frequency. Unfortunately, this approach cannot be applied to the partitioning of power, which must be evaluated for all the frequencies for which correlation data are available. An assessment of the dispersive properties of surface waves for different modes can be achieved more economically by estimating the signal power in the p - f domain (e.g. Louie 2001; Petrosino *et al.* 2002), however, such a task is beyond the scope of the present study.

Thirdly, another assumption made to retrieve the dispersion relationships from the data concerns the stochastic nature of the observed surface wavefield. Bursts of body waves contributing to the tremor wavefield were demonstrated in previous studies (e.g. Saccorotti *et al.* 2001b) and point to a weakness in this assumption. Mitigating this issue, however, is our observation that the body wave bursts are infrequent and of short duration, so that their importance is lessened by our consideration of long-duration windows over which the stochastic components of the wavefield are expected to dominate. Similar conclusions were reached by Chouet *et al.* (1997, 1998) in their analyses of wavefields associated with tremor and explosions at the Stromboli Volcano, Italy.

The results presented in this study are compatible with those obtained from similar analyses carried out at other volcanoes worldwide, including the Puu Oo crater (Ferrazzini *et al.* 1991), Masaya (Métiexian *et al.* 1997), Stromboli (Chouet *et al.* 1998), Somma-Vesuvius (De Luca *et al.* 1997; Saccorotti *et al.* 2001c) and Deception Island (Saccorotti *et al.* 2001a), which all point to shear wave velocities ranging between 0.3 and 0.6 km s⁻¹ at the surface and 1.5–2.0 km s⁻¹ at depths greater than 300–400 m. These similarities suggest that in spite of differences in the volcanological settings the gross mechanical properties of surficial volcanic rocks remain fairly constant.

The velocity structures obtained along the NW and SE segments of array B point to a marked velocity discontinuity at the boundary

between the inner and outer regions of the Kilauea caldera. Although weaker, a similar difference is observed between the shallow (<100 m) velocity structure imaged beneath array D, and shallow velocities imaged beneath the NW segment of array B. It is of interest to compare these results with those obtained in the inner and outer regions of other caldera structures. Data from a seismic refraction experiment conducted at the Somma–Vesuvius volcanic complex (Bruno & Rapolla 1999) indicate that compressional wave speeds in the 0–500 m depth interval range from 0.8 to 1.0 km s⁻¹ in the younger cone (Mount Vesuvius) and up to 1.5–1.9 km s⁻¹ in the older volcano (Somma). A similar velocity contrast was found at Deception Island Volcano, Antarctica (Saccorotti *et al.* 2001a). From Rayleigh phase velocities estimated at two distinct array sites, Saccorotti *et al.* (2001a) inferred a variation of roughly a factor of 2 in the shear wave velocities measured inside and outside the Deception Island caldera. Kilauea is the only case in which higher velocities are found within the caldera. At both Somma–Vesuvius and Deception Volcanoes, the velocity increases from the inner to the outer caldera regions. These differences are probably related to the particular histories of these volcanoes. For example, at Deception Island the inner caldera is submerged under the sea and is filled by loose epiclastic marine deposits the shear moduli of which are significantly lower than those of the pyroclastic and lava flow deposits constituting the pre-collapse volcanic edifice.

These considerations suggest that caldera boundaries are marked by significant lateral velocity discontinuities, and that these lateral velocity variations may be detected by inversions of the dispersion characteristics of surface waves in background noise of volcanic or cultural origin. The simple and economic procedure used in the present study may therefore be useful to map caldera boundaries in deeply eroded calderas or in calderas that are buried under successive deposits. Detailed structural mapping using this method may represent a significant step toward quantitative evaluations of the size and location of magma reservoirs active at the time of caldera-forming events, and may be critical to the assessment of the eruptive potential in quiescent volcanoes.

ACKNOWLEDGMENTS

We are indebted to Philippe Lesage, whose careful revision and thoughtful comments helped greatly in improving the quality of the manuscript. We are grateful to Y. Ida, T. Iwasaki, N. Gyoda, J. Oikawa, M. Ichihara, Y. Goto, T. Kurihara, M. Udagawa, and K. Yamamoto of the Earthquake Research Institute, University of Tokyo; K. Yamaoka, M. Nishihara, and T. Okuda of Nagoya University; H. Shimizu and H. Yakiwara of Kyushu University; E. Fujita of the National Research Institute for Earth Science and Disaster Prevention, Tsukuba; T. Ohminato of the Geological Survey of Japan, Tsukuba; S. Adachi of Hakusan Corporation; C. Dietel and P. Chouet of the US Geological Survey, Menlo Park; P. Okubo, A. Okamura, M. Lisowski, M. Sako, K. Honma, and W. Tanigawa of the US Geological Survey, Hawaiian Volcano Observatory; S. McNutt, D. Christensen, and J. Benoit of the University of Alaska, Fairbanks; and S. Kedar of the California Institute of Technology, Pasadena, for their participation in the field experiment. In particular, we wish to thank Y. Ida, whose exceptional organizational skills made this experiment possible. Funding for the experiment was provided by a grant from the Japanese Ministry of Education (Monbusho) to the Earthquake Research Institute of the University of Tokyo. Gaetano De Luca is acknowledged for invaluable help provided during the initial phase of our analyses.

REFERENCES

- Aki, K., 1957. Space and time spectra of stationary stochastic waves, with special reference to microtremors, *Bull. Earthq. Res. Inst. Tokyo Univ.*, **25**, 415–457.
- Aki, K., 1965. A note on the use of microseisms in determining the shallow structures of the Earth's crust, *Geophysics*, **30**, 665–666.
- Aki, K., Chouet, B., Fehler, M., Zandt, G., Koyanagi, R., Colp, J. & Hay, R.G., 1978. Seismic properties of a shallow magma reservoir in Kilauea Iki by active and passive experiments, *J. geophys. Res.*, **83**, 2273–2282.
- Almendros, J., Chouet, B.A. & Dawson, P.B., 2001. Spatial extent of a hydrothermal system at Kilauea Volcano, Hawaii, determined from array analyses of shallow long-period seismicity, 2, Results, *J. geophys. Res.*, **106**, 13 580–13 597.
- Benz, H.M., Chouet, B.A., Dawson, P.B., Lahr, J.C., Page, R.A. & Hole, J.A., 1996. Three-dimensional *P* and *S* wave velocity structure of Redoubt Volcano, Alaska, *J. geophys. Res.*, **101**, 8111–8128.
- Bettig, B., Bard, P.Y., Scherbaum, F., Riepl, J., Cotton, F., Cornou, C. & Hatzfeld, D., 2001. Analysis of dense array noise measurements using the modified spatial autocorrelation method (SPAC). Application to the Grenoble area. *Boll. Geof. Teor. Appl.*, **42**, 15–27.
- Bruno, P.P.G. & Rapolla, A., 1999. Study of the sub-surface structure of Somma–Vesuvius (Italy) by seismic refraction data, *J. Volc. Geotherm. Res.*, **92**, 373–387.
- Chiarabba, C., Amato, A., Boschi, E. & Barberi, F., 2000. Recent seismicity and tomographic modeling of the Mt Etna plumbing system, *J. geophys. Res.*, **105**, 10 923–10 938.
- Chouet, B.A., 1996. New methods and future trends in seismological volcano monitoring, in *Monitoring and Mitigation of Volcano Hazards*, pp. 23–97, eds Scarpa, R. & Tilling, R.I., Springer, Berlin.
- Chouet, B.A. & Dawson, P.B., 1997. Observations of very-long-period impulsive signals accompanying summit inflation of Kilauea Volcano, Hawaii, in February 1997, *EOS, Trans. Am. geophys. Un.*, **78** (Supplement), F429–F430.
- Chouet, B.A., Saccorotti, G., Martini, M., Dawson, P.B., Milana, G., De Luca, G. & Scarpa, R., 1997. Source and path effects in the wavefields of tremor and explosions at Stromboli volcano, Italy, *J. geophys. Res.*, **102**, 15 129–15 150.
- Chouet, B., De Luca, G., Milana, G., Dawson, P., Martini, M. & Scarpa, R., 1998. Shallow velocity structure of Stromboli volcano, Italy, derived from small-aperture array measurements of Strombolian tremor, *Bull. seism. Soc. Am.*, **88**, 653–666.
- Chouet, B. *et al.*, 2002. Source mechanisms of explosions at Stromboli Volcano, Italy, determined from moment-tensor inversions of very-long-period data, *J. geophys. Res.*, in press.
- Dawson, P.B., Chouet, B.A., Okubo, P.G., Villasenor, A. & Benz, H.M., 1999. Three-dimensional velocity structure of the Kilauea Caldera, Hawaii, *Geophys. Res. Lett.*, **26**, 2805–2808.
- De Luca, G., Scarpa, R., Del Pezzo, E. & Simini, M., 1997. Shallow structure of Mt Vesuvius volcano, Italy, from seismic array analysis, *Geophys. Res. Lett.*, **24**, 481–484.
- Del Pezzo, E., Bianco, F. & Saccorotti, G., 2001. Separation of intrinsic and scattering *Q* for volcanic tremor: an application to Etna and Masaya volcanoes, *Geophys. Res. Lett.*, **28**, 3083–3086.
- Ferrazzini, V., Aki, K. & Chouet, B., 1991. Characteristics of seismic waves composing Hawaiian volcanic tremor and gas-piston events observed by a near-source array, *J. geophys. Res.*, **96**, 6199–6209.
- Furumoto, M., Kunitomo, T., Inoue, H., Yamada, I., Yamaoka, K., Ikami, A. & Fukao, Y., 1990. Twin sources of high-frequency volcanic tremor of Izu-Oshima volcano, Japan, *Geophys. Res. Lett.*, **17**, 25–27.
- Gardner, G.H.F., Gardner, L.W. & Gregory, A.R., 1974. Formation velocity and density—the diagnostic basis for stratigraphic traps, *Geophysics*, **39**, 770–780.
- Goldstein, P. & Chouet, B., 1994. Array measurements and modeling of sources of shallow volcanic tremor at Kilauea Volcano, Hawaii, *J. geophys. Res.*, **99**, 2637–2652.
- Herrmann, R.B., 1987. Surface wave inversion program, St Louis University, St Louis, MO.

- Koyanagi, R.Y., Chouet, B.A. & Aki, K., 1987. Origin of volcanic tremor in Hawaii. Part 1, in *Volcanism in Hawaii*, Vol. 1350, pp. 1221–1257, eds Decker, R.W., Wright, T.L. & Stauffer, P.H., US Geol. Surv. Prof. Pap.
- Liu, H.P., Boore, D.M., Joyner, W.B., Oppenheimer, D.H., Warrick, R.E., Zhang, W., Hamilton, J.C. & Brown, L.T., 2000. Comparison of phase velocities from array measurements of Rayleigh waves associated with microtremor and results calculated from borehole shear wave velocity profiles, *Bull. seism. Soc. Am.*, **90**, 666–678.
- Louie, J.N., 2001. Faster, better: shear-wave velocity to 100 meters depth from refraction microtremor arrays, *Bull. seism. Soc. Am.*, **91**, 347–364.
- McNutt, S.R., Ida, Y., Chouet, B.A., Okubo, P.G., Oikawa, J. & Saccorotti, G., 1997. Kilauea volcano provides hot seismic data for joint Japanese–US Experiment, *EOS, Trans. Am. geophys. Un.*, **78**, 105–107.
- Menke, W., 1989. *Geophysical Data Analysis: Discrete Inverse Theory*. Academic Press, New York.
- Métaxian, J.-P., Lesage, P. & Dorel, J., 1997. Permanent tremor at Masaya Volcano, Nicaragua: wavefield analysis and source location, *J. geophys. Res.*, **102**, 22 529–22 545.
- Mora, M., Lesage, P., Dorel, J., Bard, P., Métaxian, J.P., Alvarado, G.E. & Leandro, C., 2001. Study of seismic site effects using H/V spectral ratios at Arenal Volcano, Costa Rica, *Geophys. Res. Lett.*, **28**, 2991–2993.
- Nakamura, Y., 1989. A method for dynamic characteristics estimation of subsurface using microtremor on the ground surface, *Q. Rep. Railway Tech. Res. Inst.*, **30**, 25–33.
- Nishimura, T. *et al.*, 2000. Source process of very long period seismic events associated with the 1998 activity of Iwate Volcano, northeastern Japan, *J. geophys. Res.*, **105**, 19 135–19 147.
- Ohminato, T., Chouet, B.A., Dawson, P.B. & Kedar, S., 1998. Waveform inversion of very long period impulsive signals associated with magmatic injection beneath Kilauea Volcano, Hawaii, *J. geophys. Res.*, **103**, 23 839–23 862.
- Okubo, P.G., Benz, H.M. & Chouet, B.A., 1997. Imaging the crustal magma sources beneath Mauna Loa and Kilauea volcanoes, Hawaii, *Geology*, **25**, 867–870.
- Petrosino, S., Cusano, P., Saccorotti, G. & Del Pezzo, E., 2002. Seismic attenuation and shallow velocity models at Stromboli Volcano, Italy, *Bull. seism. Soc. Am.*, **92**, 1102–1116.
- Saccorotti, G., Chouet, B.A., Martini, M. & Scarpa, R., 1998. Bayesian Statistics applied to location of the source of explosions at Stromboli volcano, Italy, *Bull. seism. Soc. Am.*, **88**, 1099–1111.
- Saccorotti, G., Almendros, J., Carmona, E., Ibanez, J. & Del Pezzo, E., 2001a. Slowness anomalies from two dense seismic arrays at Deception Island Volcano, Antarctica, *Bull. seism. Soc. Am.*, **91**, 561–571.
- Saccorotti, G., Chouet, B.A. & Dawson, P.B., 2001. Wavefield properties of a shallow long-period event and tremor at Kilauea volcano, Italy, in *Mechanics and Thermal Fluid-Dynamics of Volcanic Processes*, Vol. 109, pp. 163–189, eds De Natale, G., Chouet, B.A. & Kilburn, C., *J. Volcanol. Geotherm. Res.*
- Saccorotti, G., Maresca, R. & Del Pezzo, E., 2001. Array analyses of seismic noise at Mt Vesuvius Volcano, Italy, *J. Volc. Geotherm. Res.*, **110**, 79–100.
- Xia, J., Miller, R.D. & Park, C.B., 1999. Estimation of near-surface shear-wave velocity by inversion of Rayleigh wave, *Geophysics*, **64**, 691–700.
- Yamaoka, K., Oikawa, J. & Ida, Y., 1991. An isotropic source of volcanic tremor—observation with a dense seismic array at Izu-Oshima volcano, Japan, *J. Volc. Geotherm. Res.*, **47**, 329–336.
- Zollo, A. *et al.*, 1996. Seismic evidence for a low-velocity zone in the upper crust beneath Mount Vesuvius, *Science*, **274**, 592–594.

